Ocean Engineering 147 (2018) 386–398

Contents lists available at ScienceDirect

Ocean Engineering

journal homepage: www.elsevier.com/locate/oceaneng

Asymmetric water impact of a two dimensional wedge: A systematic numerical study with transition to ventilating flow conditions

Vesselin K. Krastev *, Andrea L. Facci, Stefano Ubertini

Department of Economics, Engineering, Society and Business Organization, University of Tuscia, 01100 Viterbo, Italy

ARTICLE INFO

Keywords:
Asymmetric water impact
Hull slamming
Computational Fluid Dynamics
Volume Of Fluid

ABSTRACT

Vessels and other marine structures are frequently subject to intense loads deriving from water impact under various conditions. Such forces influence both the structural resistance and the maneuvering capabilities of boats. Water impacts are also relevant in other fields, such as civil engineering, energy harvesting, and aerospace engineering.

In this paper we numerically investigate the hydrodynamics related to the asymmetric water impact of a two dimensional wedge shape. We study the combined effects of geometrical and kinematic asymmetry by systematically varying the wedge roll angle and the direction of the impact velocity. The Volume Of Fluid (VOF) is utilized to model the free surface flow. The numerical model is validated against independent experimental data available in the literature.

The results provided evidence the capabilities of multidimensional modeling in predicting global hydrodynamics and local fluid dynamics features of asymmetric impacts. Moreover, we demonstrate the importance of some fundamental methodological aspects, such as the correct initialization of the computational domain. The role of kinematic asymmetry in flow ventilation occurrence is also clearly highlighted. Our results are expected to facilitate the development of analytical and semi-analytical models and to offer guidelines for conducting experiments and parametric studies for the design of marine vessels.

1. Introduction

The fluid dynamic processes related to water entry problems are of great interest for ship design (Abrate, 2011) and other engineering applications, such as aerospace (Seddon and Moatamedi, 2006) and off-shore structures (Faltinsen, 1993; Facci et al., 2016). Special attention has been given to the hull slamming phenomenon, which usually occurs when a high speed planing boat hull or a sea plane impacts the water (Abrate, 2011; Faltinsen et al., 2004). The generated fluid flow is quite complex and includes free surface piercing and deformation, water sprays, air entrainment and, under some circumstances, flow separation and ventilation (Judge et al., 2004; Shams et al., 2015). All these aspects significantly influence the maneuvering characteristics, as well as the hydrodynamic loading and, consequently, structural fatigue behavior of marine vessels (Gu and Moan, 2002; Faltinsen et al., 2004; Silva and Ravichandran, 2012). A special case is represented by asymmetric impacts which are typical of heeled or yawed planing hulls and, at high speeds, can produce dynamic instability effects which still have to be fully understood (Judge et al., 2004). Impact asymmetry can also occur when any kind of vessel moves with multiple degrees of freedom into steep waves.

Attempts of solving analytically the slamming problem were initially focused on the hydrodynamic load estimation for two-dimensional wedge-like vertical entry configurations (Von Kármán, 1929; Wagner, 1932). These early studies were then progressively extended to different hull geometries and adding more physics to the underlying basic assumptions (Dobrovol'skaya, 1969; Cointe and Armand, 1987; Cointe, 1989; Cointe, 1991; Howinson et al., 1991; Greenhow, 1987). Most of these studies are focused on vertical symmetric impacts. Although still elegant in their formulation, the few known analytical studies on asymmetric water entry (Korobkin, 1988; Miloh, 1991; Chekin, 1989) are generally not meant to describe the asymmetry-generated flow separation and ventilation.

Most known experimental works on the water entry are also limited to symmetric impacts (Tveitnes et al., 2008; Charca et al., 2009; Lewis et al., 2010; Battley and Allen, 2012; Panciroli et al., 2015a; Russo et al., 2017). Remarkable exceptions can be found in (Judge et al., 2004) and in the work from (Shams et al., 2015) which takes benefit from some

* Corresponding author.
E-mail addresses: v.krastev@unitus.it, v.krastev84@gmail.com (V.K. Krastev).

https://doi.org/10.1016/j.oceaneng.2017.10.048
Received 10 April 2017; Received in revised form 16 July 2017; Accepted 22 October 2017
Available online 5 November 2017

recently developed PIV-based pressure reconstruction techniques (Panciroli and Porfiri, 2013; Jalalisendi et al., 2015; Jalalisendi and Osma, 2015; Panciroli et al., 2015b; Russo et al., 2016). Experimental findings pointed out some differences between geometrical and kinematic asymmetry during the water entry (Judge et al., 2004) and allowed to classify the asymmetric impacts depending on the ventilation occurrence on the low pressure side of the wedge (Judge et al., 2004; Shams et al., 2015).

Numerical solutions are powerful tools to efficiently complement experimental measurements in fluid-structure interaction problems. Currently available methods for the simulation of free surface flows include Boundary Element Method (BEM) (Zhao and Faltinsen, 1993; Lu et al., 2000; Wu et al., 2004; Wu, 2007; Xu et al., 2008), Smoothed Particle Hydrodynamics (SPH) (Shao et al., 2006; Oger et al., 2006; Shadloo et al., 2016), Lattice-Boltzmann (LB) (Falcucci et al., 2011; Zarghami et al., ; De Rosis et al., 2014) and Navier-Stokes (NS) solvers. Additionally, several types of mesh based NS approaches can be found in the scientific literature, such as the Volume Of Fluid (VOF), Level Set (LS) or Artificial Compressibility (AC) methods (Hirt and Nichols, 1981; Osher and Sethian, 1988; Kelecy and Pletcher, 1997; De Jouëtte et al., 2001; Carrica et al., 2010; Chung, 2013; Ma et al., 2015). Recent applications of VOF to symmetric water entry problems can be found in (Facci et al., 2015; Facci and Ubertini, 2015). A two fluid LS method is proposed in (Gu et al., 2014) and utilized to study the water entry of two-dimensional (2D) rigid shapes showing a qualitatively consistent behavior. To the best of our knowledge a systematic validation of CFD models for different oblique entry configurations and an insight on the physical and geometrical parameters which influence the transition from non-ventilating to ventilating flow are missing in the scientific literature.

This paper presents a detailed numerical study of a wedge-like two-dimensional section impacting water surface under a variety of geometrical and kinematic asymmetry conditions. The simulations are performed through a VOF-based algorithm (Rider and Kothe, 1998; Scardovelli and Zaleski, 1999; Rusche, 2002), coupled with a Laplacian mesh-motion solver (Jasak and Tukovic, 2007; Jasak, 2009; Kassiotis, 2008), already employed and validated for symmetric water entry problems (Facci et al., 2015; Facci and Ubertini, 2015). The paper is organized as follows. The main features of the problem in study are described in Section 2. Then, a focus on the numerical approach, including details on the computational domain and numerical setup is given in Section 3.1. In Section 4 the methodology is validated by comparing present numerical results to literature experimental data (Judge et al., 2004). The hydrodynamics related to the water impact is discussed in Section 5. Conclusions are drawn in Section 6.

2. Problem statement

In this paper we investigate the two dimensional hydrodynamics related to the asymmetric water impact of a rigid wedge through Computational Fluid Dynamics (CFD).

The problem is schematically represented in Fig. 1, which reports the relevant characteristics of the specimen and of the fluid flow. The geometry of the wedge is defined in terms of its width $l = 0.20$m, height $h = 0.08$m, and dead-rise angle $\beta = 37^{\circ}$. Such a geometry is selected to reproduce the experiments described by (Judge et al., 2004).

We hypothesize that the wedge breadth is much larger compared to l and to h, such that the geometry, and the hydrodynamics can be considered two dimensional (Jalalisendi et al., 2015). A fixed Cartesian reference frame is selected with the $x-$axis along the horizontal direction (i.e. along the water free surface) and the $y-$axis along the vertical direction.

The hull keel impacts on the water surface at the origin of the reference frame and at time $t = 0$ s. We denote with $\varepsilon(t)$ the abscissa of the wedge keel and with $\xi(t)$ its ordinate at time t. The wedge kinematics is defined by its constant velocity $\boldsymbol{v} = (\dot{\varepsilon}, \dot{\xi})$ being the superimposed dot the time derivative, and by the constant roll angle θ. The velocity ratio $\tau = \dot{\varepsilon}/\dot{\xi}$ quantitatively represents the kinematic asymmetry of the water entry, and the angle θ represents the geometrical asymmetry.

We assume that the two fluids (air and water) are immiscible and the flow is incompressible. Thereafter, the flow field is described by the mass conservation and momentum balance equations, as follows:

$$\nabla \cdot \boldsymbol{u} = 0, \tag{1a}$$

$$\frac{\mathrm{D}(\rho \boldsymbol{u})}{\mathrm{D}t} = -\nabla p + \nabla \cdot \mu \nabla \boldsymbol{u} + \rho \boldsymbol{g}, \tag{1b}$$

where $\boldsymbol{u}$ is the fluid velocity, p is the pressure, μ is the dynamic viscosity, ρ is the density, $\boldsymbol{g}$ is the gravitational acceleration, and $\mathrm{D}(\cdot)/\mathrm{D}t$ denotes the material derivative. Note that ρ and μ vary in space and time according to the fluid phase, air or water. In particular, the air density and viscosity are $\rho_{\mathrm{a}} = 1\mathrm{kg/m^3}$ and $\mu_{\mathrm{a}} = 1.48 \times 10^{-5}$Pa s, respectively, and the water density and viscosity are $\rho_{\mathrm{w}} = 1000\mathrm{kg/m^3}$ and $\mu_{\mathrm{w}} = 1 \times 10^{-3}$Pa s, respectively.

Experimental observations show that for low τ and θ the flow remains attached on both sides of the wedge (Judge et al., 2004; Shams et al., 2015), as qualitatively represented in Fig. 1a, and the flow asymmetry is defined by the ratio $b^* = b_2/b_1$, where b_1 and b_2 are the jet root abscissa on the lower and upper side of the wedge respectively. As in (Judge et al., 2004), from now on we will refer to such a flow as type A flow. Increasing the asymmetry (i. e. decreasing b^*), a cavity should appear on the upper side of the hull (see Fig. 1b) and the flow is denoted as type B flow (Judge et al., 2004).

The encompassing fluid reacts to the wedge motion generating a force that can be expressed as:

$$\boldsymbol{F} = \int_{\Sigma} \{ -p\boldsymbol{I} + \mu[\nabla \boldsymbol{u} - \nabla \boldsymbol{u}^{\mathrm{T}}] \} \boldsymbol{n} \mathrm{d}\Sigma, \tag{2}$$

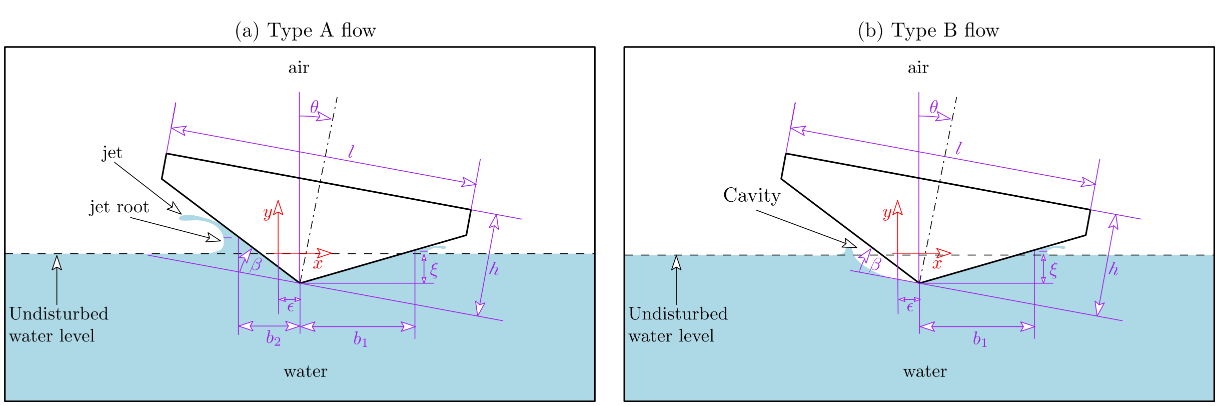

Fig. 1. Schematic representation of the problem in study for the two limiting flow conditions.

where $\boldsymbol{I}$ is the identity matrix, Σ is the hull surface, and $\boldsymbol{n}$ is the unit normal to the hull. We define the moment of $\boldsymbol{F}$ with respect to the wedge keel as:

$$\boldsymbol{M} = \int_{\Sigma} \boldsymbol{d} \times \{ -p\boldsymbol{I} + \mu[\nabla\boldsymbol{u} - \nabla\boldsymbol{u}^{\mathrm{T}}] \} \boldsymbol{n} \mathrm{d}\Sigma, \tag{3}$$

being $\boldsymbol{d}$ the position vector evaluated from the keel itself.

With reference to Fig. 1, the geometrical wetted length projection onto the undisturbed water line is defined as:

$$l_w = \xi(t) \cdot \left(\frac{1}{tan(\beta - \theta)} + \frac{1}{tan(\beta + \theta)} \right) \tag{4}$$

Considering l_w and $|\boldsymbol{v}|$ as the impact characteristic length and velocity scales, we define the following non-dimensional force and moment coefficients:

$$C_{Fx} = \frac{2F_x}{\rho_w |\boldsymbol{v}|^2 l_w} \tag{5}$$

$$C_{Fy} = \frac{2F_y}{\rho_w |\boldsymbol{v}|^2 l_w} \tag{6}$$

$$C_{Mz} = \frac{2M_z}{\rho_w |\boldsymbol{v}|^2 l_w^2} \tag{7}$$

with F_x, F_y and M_z being the force components and tilting moment per unit span, respectively. To study pressure variations during water entry we also introduce the following non-dimensional pressure coefficient:

$$C_p = \frac{2(p - p_\infty)}{\rho_w |\boldsymbol{v}|^2} \tag{8}$$

with p_∞ being the air pressure at ambient conditions. Finally, we define the impact characteristic Reynolds number as:

$$Re = \frac{\rho_w |\boldsymbol{v}| \cdot \delta_{ref}}{\mu_w} \tag{9}$$

where δ_{ref} is a reference value of the keel penetration along the impact direction.

3. Methodology

3.1. Numerical method

We numerically study the flow induced by the wedge motion through a method based on a special VOF implementation (Rider and Kothe, 1998; Scardovelli and Zaleski, 1999; Rusche, 2002) that is included in the OpenFOAM-2.4 CFD package (OpenFOAM, 2015). Similar applications of such a method are, for instance (Facci et al., 2015, 2016; Facci and Ubertini, 2015; Cavalagli et al., 2017), The incompressible flow of two immiscible fluids is modeled through a single set of the Navier-Stokes and continuity equations (see eq. (1)). The interface between the two phases is defined solving Eq. (10) (Rusche, 2002):

$$\frac{\mathrm{D}\alpha}{\mathrm{D}t} + \nabla \cdot [\boldsymbol{u}_r \alpha (1 - \alpha)] = 0, \tag{10}$$

where α is the water volume fraction and $\boldsymbol{u}_r$ is the relative velocity of the two phases. The second term of Eq. (10) is introduced to compensate the numerical smearing of the fluid interface (Rusche, 2002).

Equations (1) and (10) are discretized through a generalized unstructured finite volume approach with a collocated arrangement of all the flow variables (Ferziger and Perić, 2002; Greenshields, 2015a). The pressure velocity coupling and the non linearity of Eq. (1) are solved using the Pressure Implicit with Split Operators (PISO) algorithm (Issa, 1985), keeping the original two-stage pressure correction scheme for each time integration step Δt. The discrete version of Eq. (10) is solved through the Multidimensional Universal Limiter with Explicit Solution (MULES) procedure (Greenshields, 2015b). The solution of Eq. (10) is sub-cycled in four steps for each Δt, and it is linearized using two additional steps of a fixed point iteration.

Temporal integration is performed through the Euler implicit method (Greenshields, 2015b). The Gaussian integration with second-order linear interpolation is adopted for all the spatial terms other than the convective ones. For the latter a high-resolution NVD scheme (Jasak et al., 1999) is utilized to balance numerical stability and accuracy. Depending on the local flow conditions, this scheme bridges the standard second-order central differencing with first-order upwind differencing by means of a specifically designed nonlinear function. A smoothness factor γ controls the behavior of the bridging function, where $\gamma = 0$ corresponds to pure central differencing and $\gamma = 1$ to the maximum boundedness level. Here we set $\gamma = 0.2$, which means that central differencing is applied in most of the cases.

The motion of the wedge within the computational domain is obtained by reallocating the mesh nodes at each time step. Topology modifications are not allowed. The grid deformation is performed using the Laplace smoothing methodology (Jasak and Tukovic, 2007; Jasak 2009; Kassiotis, 2008), assuming a diffusivity coefficient distribution that concentrates most of the deformation away from the wedge surface.

The linear systems of equations resulting from temporal and spatial discretization are solved using the Geometric Agglomerated Algebraic Multi Grid (GAMG) iterative algorithm for pressure and the Gauss-Seidel method for other scalar quantities (Greenshields, 2015b).

We comment that turbulence modeling is not required for the numerical solution of the hull-slamming problem. In fact, the impulsive nature of the water entry related phenomena does not allow the development of a proper energy cascade as demonstrated by (Seng et al., 2012). The same consideration applies also for three dimensional effects (Seng et al., 2012), that may only derive from edge effects that can be safely discarded when the transversal dimension of the falling body is much larger than the other ones, as we assume, without loosing generality, in the present study.

3.2. Domain discretization and boundary conditions

A domain of dimensions 2m × 2m is considered to minimize the effects of the imposed boundary conditions on the fluid flow in the vicinity of the hull. The domain is discretized through the OpenFOAM®built-in meshing tool *snappyHexMesh*, which is able to generate unstructured but highly hexa-dominant grids with optional layer generation at the solid surfaces. Regardless of the θ value, all the employed meshes have the following common characteristics (see Fig. 2):

(i) A background spacing level, which covers most of the domain; (ii) a first refinement zone, extending from the left to the right wall and including the falling wedge and the whole free surface; (iii) a second refinement zone, placed below the lower surfaces of the wedge and covering the free surface portion that is actually affected by the impact; (iv) a third refinement zone, represented by a 1 cm wide belt around the wedge; (v) three low aspect-ratio extrusion layers at the walls of the wedge.[1]

Boundary conditions are set following the conclusions of previous computational studies (Facci et al., 2015, 2016; Facci and Ubertini, 2015). The domain is considered as a tank with free-slip walls and an open end on top. Table 1 summarizes the BC settings for pressure,

[1] In single-phase flows highly stretched wall layers are commonly introduced to solve boundary layers, assuming that gradients in the wall-normal direction are the most relevant ones. In VOF solvers stretched cells should be avoided, as they tend to produce an inconsistently biased transport of the liquid volume fraction.

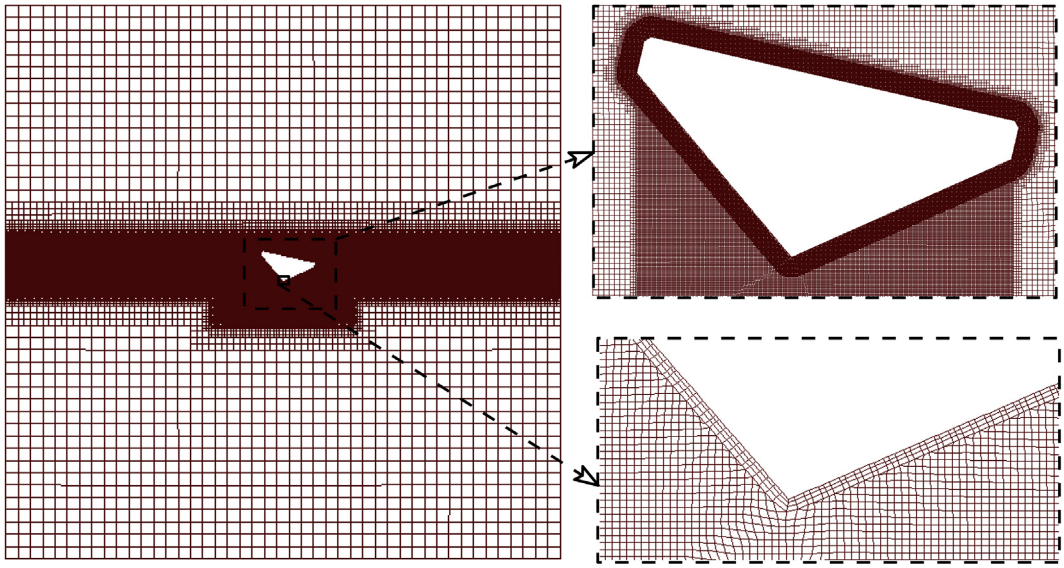

Fig. 2. Example of the computational grids utilized for the simulations.

Table 1
Boundary conditions adopted for the simulations.

Boundary	Pressure BC	Velocity BC	α BC
Top	$p = p_\infty$	$\boldsymbol{n}\cdot\nabla\boldsymbol{u} = 0$	$\boldsymbol{n}\cdot\nabla\alpha = 0$ (out), $\alpha = 0$ (in)
Bottom	$\boldsymbol{n}\cdot\nabla p = 0$	free slip	$\boldsymbol{n}\cdot\nabla\alpha = 0$
Right	$\boldsymbol{n}\cdot\nabla p = 0$	free slip	$\boldsymbol{n}\cdot\nabla\alpha = 0$
Left	$\boldsymbol{n}\cdot\nabla p = 0$	free slip	$\boldsymbol{n}\cdot\nabla\alpha = 0$
Wedge	$\boldsymbol{n}\cdot\nabla p = 0$	$\boldsymbol{u} = \boldsymbol{v}$	$\boldsymbol{n}\cdot\nabla\alpha = 0$

velocity and the liquid volume fraction α. Note that to avoid backflow phenomena the α BC at the open end changes its behavior depending on the flux direction.

4. Validation

In this Section we compare our numerical results with experimental measurements collected by (Judge et al., 2004) on various asymmetric impact configurations. Table 2 shows the configurations considered for this validation stage, in terms of the velocity ratio τ and rolling angle θ. The impact velocity magnitude varies between 2 m/s and 5 m/s depending on the τ value (Judge).

4.1. Effects of grid refinement and initial conditions

Preliminary computations are made to check the effects of grid refinement and domain initialization. At this point τ and θ are fixed to 0.75 and 26°, respectively. Experimental evidence has shown that these values should produce a type B flow, close to the transition from non-ventilating to ventilating flow (Judge et al., 2004).

The simulations have been performed with three different computational grids, each one characterized by a different minimum cell size in the belt region (see Table 3). The water free surface is initialized at 1.6 cm below the wedge keel, and the specimen falls for 5 ms before impacting the water surface.

Table 2
Impact parameters used for the validation.

τ	θ	$\dot{\varepsilon}$ [m/s]	$\dot{\xi}$ [m/s]
0.25	9°, 13°, 19°, 22°, 26°, 30°	1.20	4.80
0.50	9°, 13°, 19°, 22°, 26°, 30°	2.05	4.10
0.75	9°, 13°, 19°, 22°, 26°, 30°	2.40	3.20
2.00	5°	2.00	1.00

Fig. 3(a–c) show the time history of the forces and tilting moment per unit span for the three considered meshes, up to 3.5 ms after the water impact and with a 0.25 ms sampling resolution. For each mesh, we calculate an average relative deviation parameter across the sampling interval, which is defined as follows:

$$\Delta\Psi[\%] = 100\cdot\frac{1}{N-1}\sum_{i=1}^{N}\left[\frac{\left|\Psi_i - \overline{\Psi}_i\right|}{\max\left(\overline{\Psi}_i\right) - \min\left(\overline{\Psi}_i\right)}\right] \quad (11)$$

where N is the number of sampling points, Ψ is alternatively F_x, F_y or M_z and the overline operator $\overline{(\cdot)}$ represents the mean of the values predicted by all meshes at a given sampling point. Table 4 collects the deviation parameters for each mesh and force component, evidencing that the overall dispersion is well below what would be typically desirable for experimental data sets. In addition to the integral forces analysis, we perform a local pressure coefficient monitoring over time at a given measuring point located on the high pressure side of the impacting wedge. Monitoring starts 5 ms before and ends 5 ms after the water impact. Fig. 3d shows the C_p time traces recorded for each mesh. It highlights a close correspondence between the medium and fine cases. Instead, the coarse mesh resolution seems not sufficient for the accurate description of the steep pressure raise that occurs right after the impact. Based on these considerations, the medium mesh is assumed as the baseline option for all the subsequent simulations.

In addition to the effects of grid refinement, we analyze the influence of the initial conditions on water impact hydrodynamics. We call type I the initialization strategy already used for the grid analysis, with the free surface placed at 1.6 cm below the keel of the wedge at the beginning of the simulation. Conversely, we call type II an alternative strategy with the keel placed exactly at the free surface when the simulation starts. Both air and water are at rest. The latter, besides being a rather common practice for the numerical simulation of water entry problems (Facci and Ubertini, 2015; Facci et al., 2015; Seng et al., 2012) might also be useful to save computational time in demanding scenarios, such as very fast impacts and/or three dimensional and complex geometrical configurations. Fig. 4 represents the water free surface for three time-steps after the impact obtained with the two initializations for $\tau = 0.75$, $\theta = 26°$. Such a configuration is ventilating (Type B flow) according to the experiments in (Judge et al., 2004). Only Type I initialization predicts the transition to type B flow. In fact, the air motion induced by falling wedge before the water entry has a crucial influence on the ventilation occurrence during

Table 3
Main characteristics of the employed numerical meshes.

	Coarse	Medium	Fine
Total cell count	~ 110000	~ 140000	~ 275000
Cells in the belt region	~ 10000	~ 40000	~ 160000
Maximum cell size (mm)	44	44	44
Minimum cell size (mm)	0.69	0.34	0.17
Number of wall layers	3	3	3
Maximum cell aspect ratio	3	3	3

the initial impact stage. On the other hand Type II initialization assumes air is at rest at the impact time, a rather unrealistic initial condition. Further tests with increased vertical pre-impact paths (3.2 cm and 6.4 cm) have shown no significant changes. Therefore, we utilize Type I initialization for all the configurations. Specifically, we assume that the specimen falls for 5 ms before entering calm water, for all configurations. The distance of the wedge keel at the beginning of the simulation varies between 0.5 cm and 2.5 cm depending on the τ value. We note that we mark the impact time with $t = 0$ s. Therefore, t represents the time after the water impact and $t = 0$ s unequivocally identifies the impact time for all the configurations.

4.2. Comparison with experimental data

The flow asymmetry ratio b^* is selected as the main validation parameter. Data sampling is made every 0.5 ms starting from water impact while, following the approach suggested by (Judge et al., 2004), the b^* value is determined from the average of 4 sequential samples as follows:

$$\overline{b^*} = \frac{1}{4}\sum_{j=3}^{7} b_j^* \tag{12}$$

where b_j^* represents the j^{th} sample. Fig. 5 shows $\overline{b^*}$ as a function of θ for three different values of τ. Present numerical results are compared with the experimental and numerical results in (Judge et al., 2004). For $\tau = 0.25$, the numerical trends are very similar and both agree well with the experiments up to $\theta = 22^\circ$. For $\theta > 22^\circ$ the measured values seem to point faster towards $\overline{b^*} = 0$, which represents the flow transition from type A to type B. For $\tau = 0.5$, our CFD simulations still well agree with the experimental trend, including the correct prediction of type B flow occurrence at $\theta = 30^\circ$. On the other hand, the numerical results from (Judge et al., 2004) generally underpredict $\overline{b^*}$, but consistently capture the flow transition to type B. The $\tau = 0.75$ graph is particularly interesting, because it shows how for large impact asymmetries (i.e. large τ and θ values) the reduced-order numerical method proposed by (Judge et al., 2004) fails to correctly describe the wetted lengths ratio and the transition to ventilation on the low pressure side of the wedge. This aspect is also commented in (Judge et al., 2004) and represents one of the main motivations for the development of multidimensional simulation methods, such as the one presented in our paper. In fact, for $\tau = 0.75$ the

Table 4
Average relative deviation of hydrodynamic forces for the different meshes, calculated according to Eq. (11).

	Coarse	Medium	Fine
ΔF_x[%]	4.9	1.7	5.6
ΔF_y[%]	1.5	1.1	1.9
ΔM_z[%]	0.8	0.7	1.5

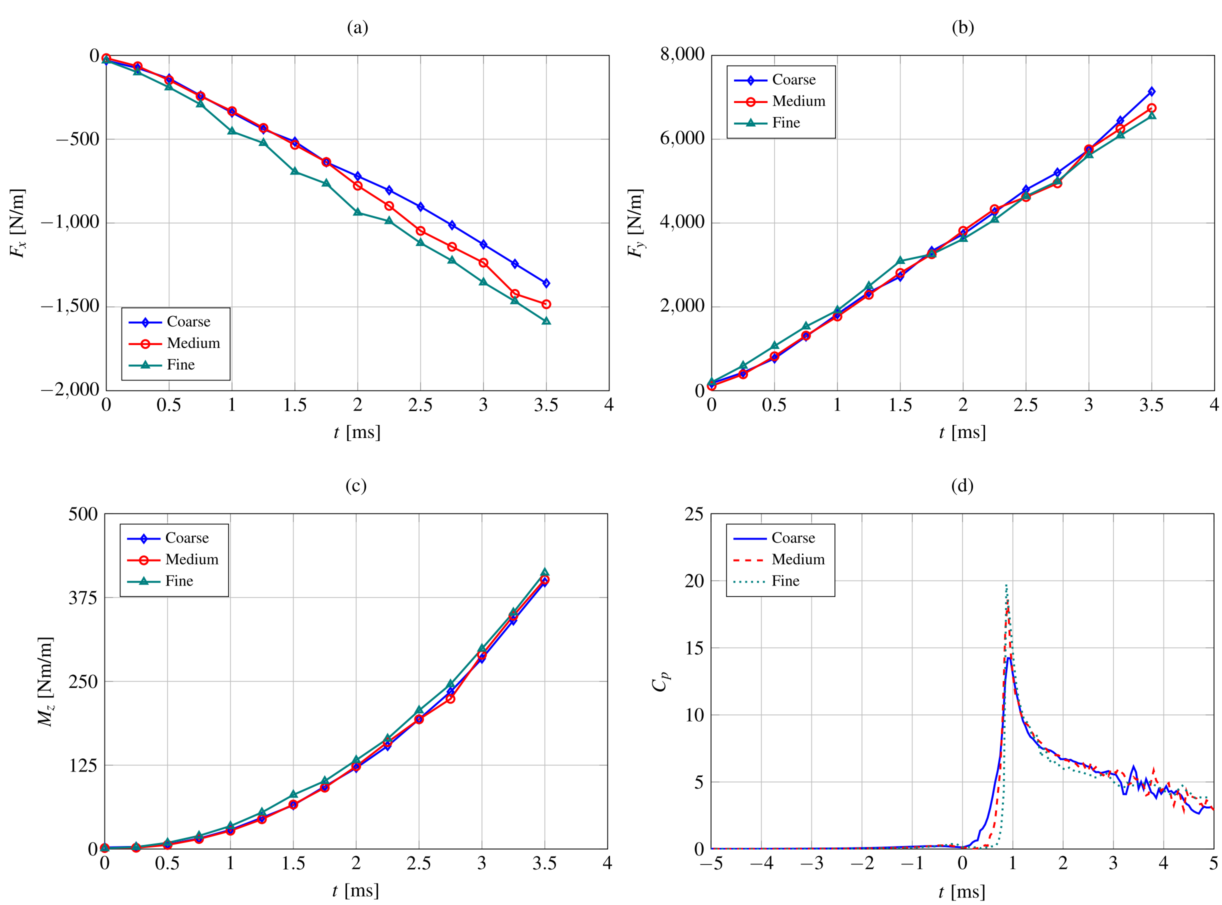

Fig. 3. Hydrodynamic forces and pressure coefficient monitor as a function of time for the three different computational meshes and for $\tau = 0.75$, $\theta = 26^\circ$.

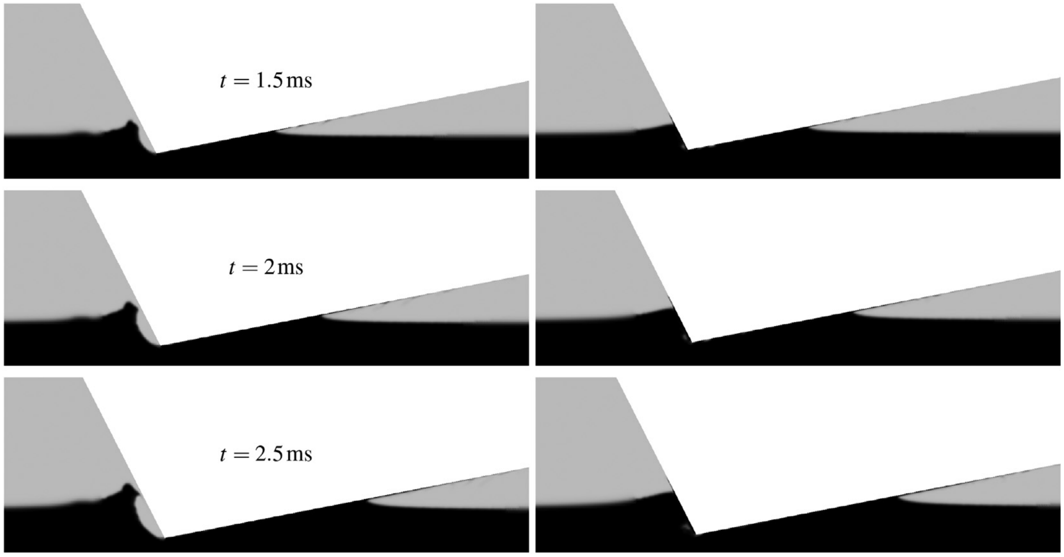

Fig. 4. Free surface evolution after water impact obtained through CFD. Comparison between type I initialization (left) and type II initialization (right).

value of $\overline{b^*}$ calculated through CFD is coherent with experimental evaluations on the whole theta range. In particular, CFD correctly capture the transition from type A to type B flow.

Further validation is provided by comparing the free surface evolution in CFD and experiments. Fig. 6 shows type A and type B flow cases, clearly highlighting that our computational model correctly predicts the pileup and the interface dynamics. In particular, for the non ventilating case, CFD correctly predicts the height of the risen water on both sides of the wedge in the considered time interval. Such an aspect is particularly relevant for the hull slamming as it largely determines the position and the value of the pressure peak on the structure. In the ventilating case CFD captures both the risen water height on the high pressure side of the wedge as well as the position and dimension of the air cavity on the low pressure side.

5. Numerical analysis of asymmetric impact

In this Section we leverage on CFD to dissect the hydrodynamics related to the asymmetric water impact in terms of hydrodynamic loading, pressure field and free surface evolution. Specifically, we seek to assess the relative effect of τ and θ on impact hydrodynamics.

5.1. Free surface dynamics

The free surface dynamics, and in particular the occurrence of flow separation, are distinctive aspects of asymmetric water impact (Judge et al., 2004). When the wedge enters the water, the free surface warps and the water level is increased with respect to the undisturbed one. Such a deformation generates the well known pileup phenomenon, that is widely studied for symmetric impacts (Wagner, 1932; Facci et al., 2015; Panciroli et al., 2015b). In case of asymmetric impacts, the effective wetted length is different on the two sides of the wedge. As already discussed in the previous Section, the flow asymmetry can be quantitatively assessed through the non-dimensional ratio, $\overline{b^*}$, reported in Fig. 5. Therein, it is shown that $\overline{b^*}$ is consistently reduced by increasing the geometrical asymmetry, for all the non ventilating cases. In fact, for a fixed penetration, the rotation of the wedge increases b_1, leaving substantially unchanged b_2, as depicted in Fig. 7. Increasing the kinematic asymmetry also reduces $\overline{b^*}$, but the kinematic asymmetry has a weaker effect on $\overline{b^*}$ compared to θ.

Both CFD and experiments demonstrate that, for $\tau = 0$, a type B flow never occurs, not even for θ as large as 30°. For $\tau = 0.5$ type B flow is obtained only for $\theta \geq 30°$, which is a very large geometrical asymmetry considered that $\beta = 37°$. Finally, for $\tau = 0.75$, a completely ventilating flow is detected for $\theta \geq 26°$, both according to CFD and to experiments (Judge et al., 2004). All these findings suggests that the ventilating cavity formation should be mostly dominated by the direction of the impact velocity relative to the geometrical symmetry axis. In a perfectly symmetric impact, the relative velocity is parallel to the symmetry axis of the wedge and two equally directed liquid jets are generated by the flow splitting at the keel. If such parallelism is broken, due to a rolling angle and/or kinematic asymmetry, one of the two jets will start aligning with the solid surface on the low pressure side. At some point the jet will be ideally parallel to the low pressure side and further changes in the impact

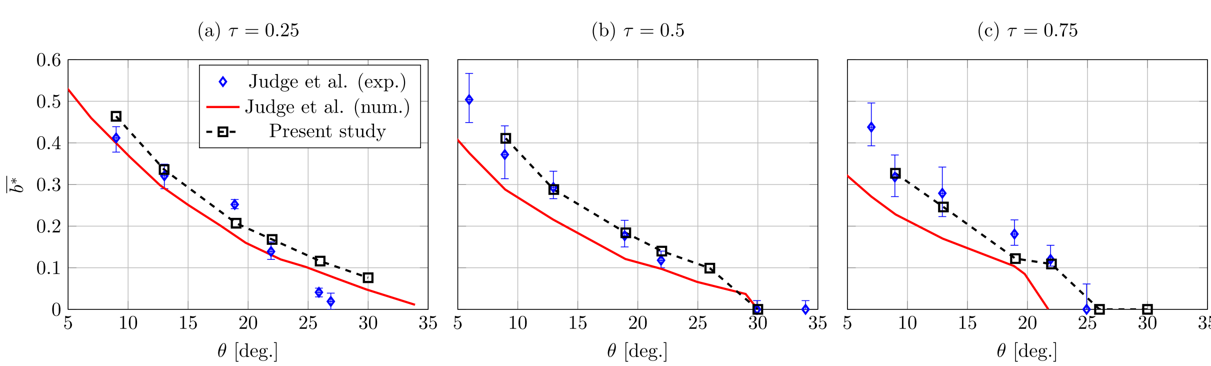

Fig. 5. Flow asymmetry as a function of τ and θ. Comparison between present results and literature experimental and numerical results.

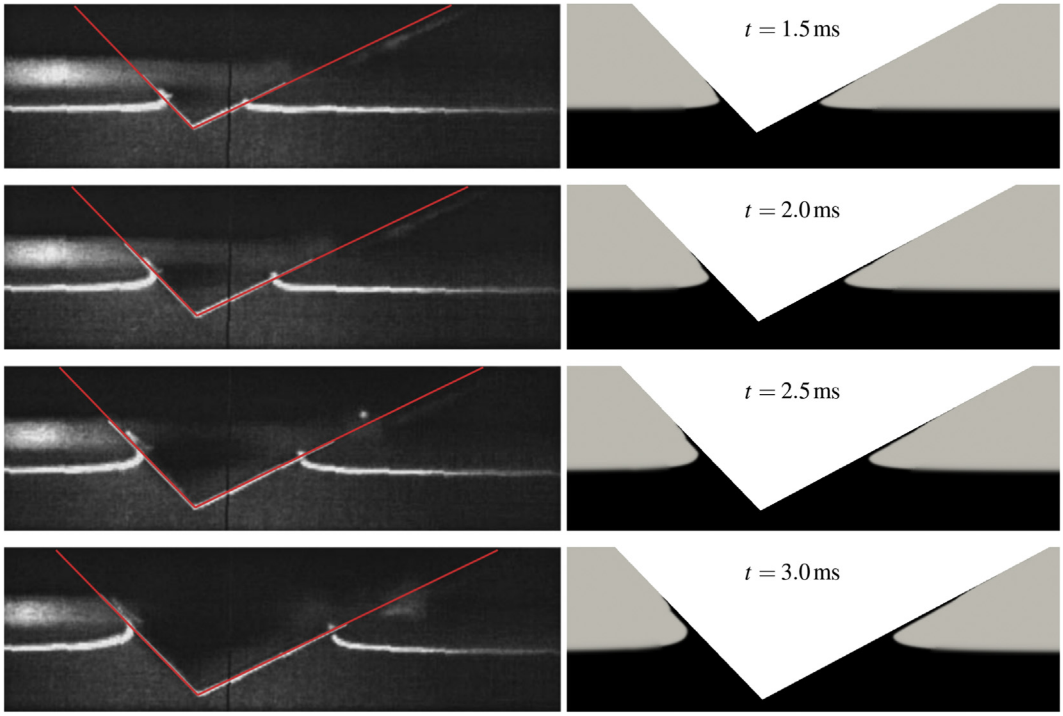

(a)

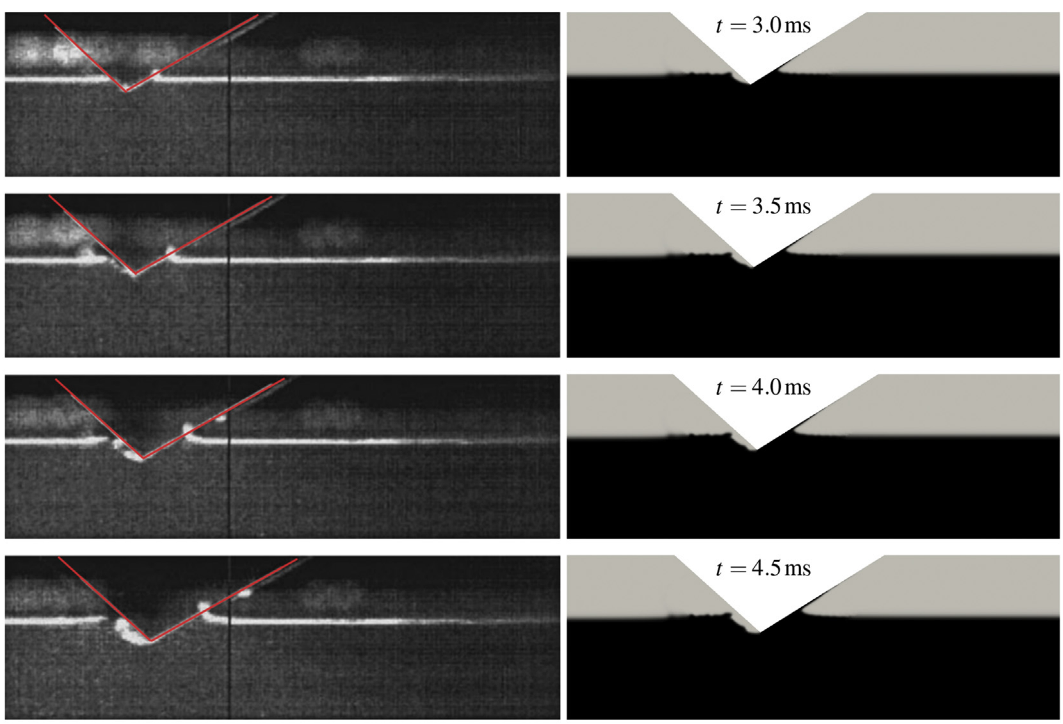

(b)

Fig. 6. Free surface evolution after water impact. Comparison between present CFD (right) and experiments from (Judge et al., 2004) (left) for: (a) type A flow, $\tau = 0.25$, $\theta = 9^{\circ}$; (b) type B flow, $\tau = 2.00$, $\theta = 5^{\circ}$.

direction will produce favorable conditions for liquid flow separation with air entrainment. For the given geometrical features of the wedge in study, such conditions cannot be apparently reached with changes in the rolling angle only.

Further details on the free surface evolution and on flow ventilation are gained from Fig. 7, which represents the free surface evolution through the water volume fraction as a function of t and θ for $\tau = 0.75$. We selected a case with a large kinematic asymmetry because it allows dissecting the transition from type A to type B flow by varying θ. For low values of θ (Fig. 7(a–d)) the flow is completely attached to the wedge surface, during the whole period of observation. Increasing the asymmetry (Fig. 7(e–h)), a small air cavity appears immediately after water impact. The cavity suddenly closes and the flow reattaches, as the penetration is increased. For $\theta = 30^\circ$ the cavity does not close during the whole simulation and the transition to type B flow is completed, as shown in Fig. 7(i–l). The role of kinematic asymmetry in promoting the transition to type B flow is also evidenced in Fig. 6 which shows that, for $\tau = 2$, flow ventilation is already obtained for θ as low as 5°.

5.2. Pressure field

Fig. 8 shows the C_p on the high pressure side of the wedge as a function of the non-dimensional wetted length and of the flow configuration. On the high pressure side C_p exhibits a self-similar behavior, analogous to the symmetric impact pressure (Facci et al., 2015; Facci and Ubertini, 2015; Panciroli et al., 2015b). Therefore, in Fig. 8 we systematically represent C_p for a single time after the impact onset (i.e. $t = 2$ ms). We comment that $y/\xi = -1$ corresponds to the wedge keel, $y/\xi = 0$ identifies the intersection between the wedge and the undisturbed water level, and $y/\xi > 0$ represents the pileup region. The contour plots of the non-dimensional pressure, depicted in Fig. 9 for $\tau = 0.75$ and as a function of t and θ, confirm the self similarity of the pressure on the high pressure side of the wedge. Note that in Fig. 9l the high pressure side of the wedge is already completely submerged (see Fig. 7). Thereafter, there is no pressure peak on the wetted surface and self similarity with the contour plots depicted in Fig. 9(i–k) is not expected. For all the considered combinations of θ and τ, the pressure peak is located at the same non-dimensional coordinate y/ξ that corresponds to the jet root location, as can be argued by comparing Figs. 9–7. The pressure peak is dramatically increased by increasing the geometrical asymmetry. Such an evidence can be interpreted noting that the larger is θ, the lower is the effective deadrise angle, and thus, the larger is the pressure peak (Wagner, 1932).

Fig. 8 shows that the pressure is significantly reduced by increasing τ. This is explained by considering that the pressure force represents the reaction of the displaced fluid to the acceleration imposed by the wedge (added mass effect). The velocity of increment of the displaced water is proportional to the vertical penetration velocity, that, in turn, decreases by increasing τ (see Table 2). On the other hand, the velocity scale selected for the definition of C_p, $|\boldsymbol{v}|$, is theoretically not influenced by the kinematic asymmetry. Experiments show only a minor reduction of $|\boldsymbol{v}|$ with τ increasing from 0 to 0.75, presumably caused by the increased friction on the experimental struts. As a consequence, C_p is reduced by increasing the kinematic asymmetry.

Fig. 9 shows that the pressures field in the low pressure side of the wedge is not self similar in time. In particular, the partially ventilating configuration (see Fig. 9e-h) is characterized by an evident low pressure zone close to the keel, that exhibits a clearly unsteady behavior. Nevertheless, to dissect the effects of kinematic and geometrical asymmetry, in Fig. 10 we systematically represent C_p on the low pressure side of the

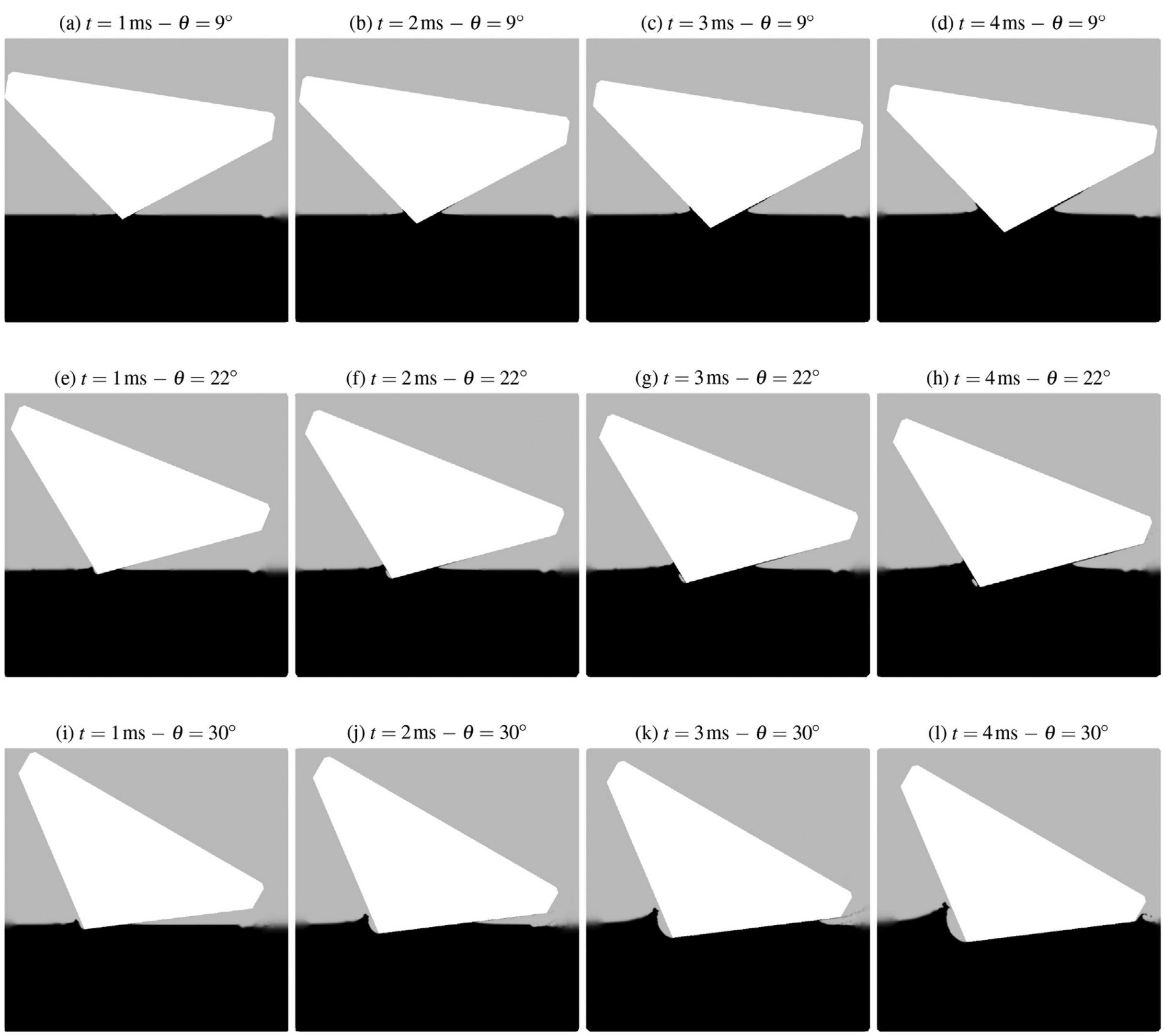

Fig. 7. Free surface evolution represented through the water volume fraction contour plots as a function of t and θ for.$\tau = 0.75$.

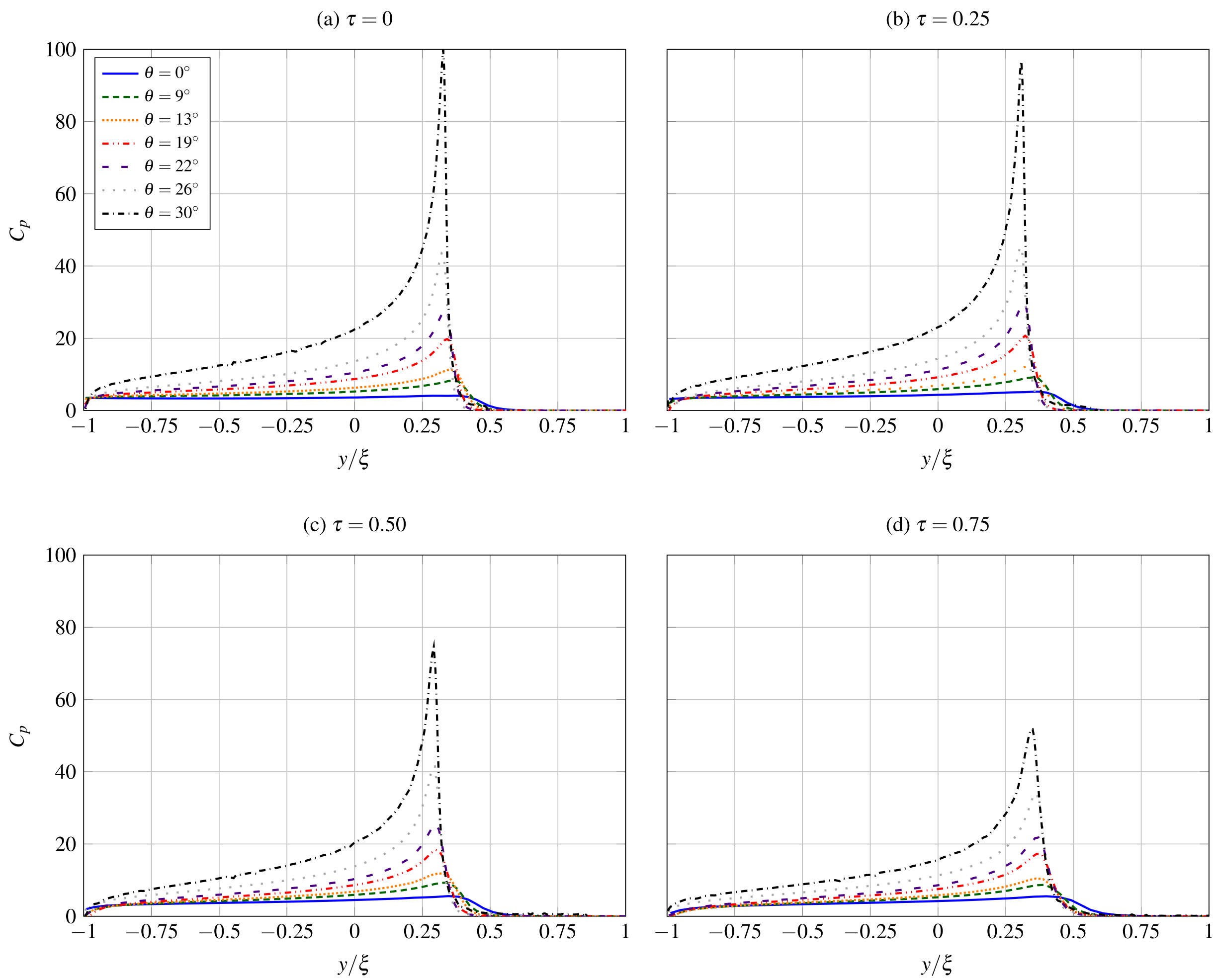

Fig. 8. Pressure profile on the wetted surface of the wedge as a function of θ and τ, high pressure side, $t = 2$ ms.

wedge as a function of τ and θ, for $t = 2$ ms. When $\theta \leq 13^{\circ}$, τ has a minor impact on C_p, with a slight progressive pressure reduction in the proximity of the keel as τ increases. This is presumably related to the increasing horizontal component of the water velocity relative to the wedge keel. In these configurations the water flow is completely attached, as, for instance, the one represented in Fig. 7. For larger θ and τ values, the pressure drop becomes stronger and extends along the wedge surface. By comparing Fig. 10 to Figs. 7 and 9 we note that such a low pressure zone is distinctive of a flow transition from type A to type B. During this transition air is trapped on the low pressure side, but without the formation of a fully ventilating cavity. After the complete transition to type B flow, that is for $\tau \geq 0.75$ and $\theta > 26^{\circ}$, the cavity is completely open and thus the pressure flattens towards the atmospheric pressure.

Fig. 11 displays the temporal evolution of C_p on the low pressure side, for $\tau = 0.75$, and should be evaluated together with Figs. 7 and 9, which show the free surface and two-dimensional pressure contours dynamics under the same flow conditions. For type A flow ($\theta = 9^{\circ}$) and for completely developed type B flow ($\theta = 30^{\circ}$), the variation of C_p in time is insignificant. On the other hand, for $\theta = 22^{\circ}$, during the flow transition from type A to type B, C_p shows an unsteady behavior. Initially, as shown in Fig. 7, the cavity is open and $p = p_{\infty}$. Afterwards, for $t \geq 2$ ms, the cavity closes (see Fig. 7) and p is reduced below atmospheric pressure. The linear dimension of the air cavity is initially larger and is gradually reduced, compared to the wedge penetration. The pressure within the closed air cavity does not vary significantly in time.

The dependence of the flow on the Reynolds number is analyzed in Fig. 12a and b, for a type A-to-type B transitional configuration ($\tau = 0.75, \theta = 26^{\circ}$). The different Re values are obtained by changing the impact velocity magnitude, while δ_{ref} is kept constant to 8×10^{-3} m. Note that $Re = 16000$ corresponds to the impact speed previously adopted for all the cases with $\tau = 0.75$. On the high pressure side, the C_p distribution reveals a substantial insensitivity to Re, which again is consistent with previous findings on symmetrical impact wedge studies (Facci and Ubertini, 2015). The low pressure side shows a relatively weak dependence on the Reynolds number, thus indicating that viscous dissipation related to the large velocity gradients at the wedge keel concurs at the pressure reduction on the low pressure side for partially ventilating configurations.

5.3. Fluid forces

The fluid force time history has been already shown in Section 4.1 for a single combination of τ and θ. To gain a better insight on how hydrodynamic loads are affected by the two types of asymmetry considered, we adopt the non-dimensional force coefficients introduced in Section 2. It is worth to note that, if the following fitting curves are used for $F(t)$ and $M(t)$

$$F(t) = at, \tag{13a}$$

$$M(t) = bt^2, \tag{13b}$$

the time dependence is effectively removed from the non-dimensional coefficients definitions. Therefore, coefficients are plotted as a function of τ and θ only.

Horizontal force trends are reported in Fig. 13a. When the asymmetry

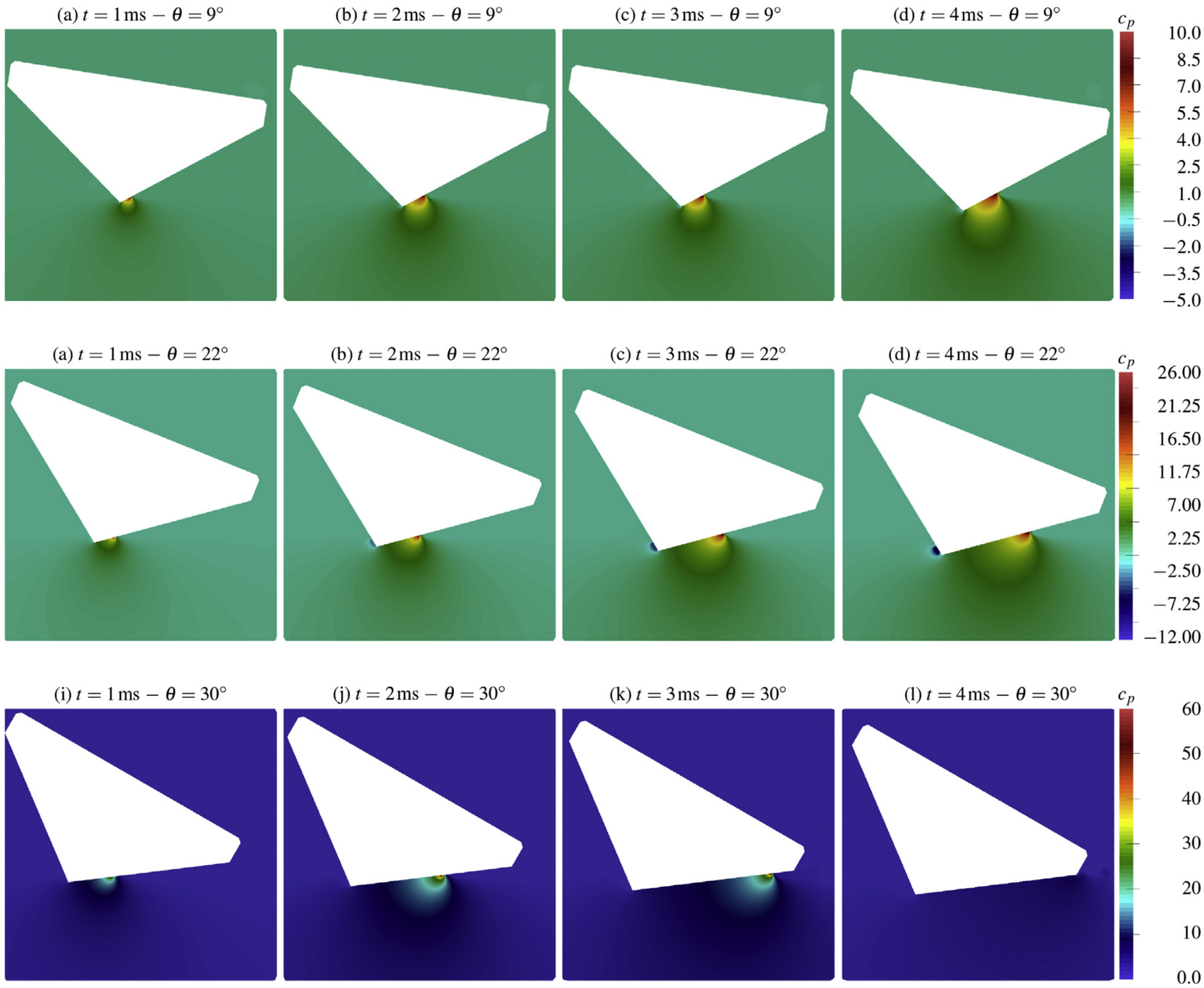

Fig. 9. Non-dimensional pressure contour plot as a function of t and θ values for $\tau = 0.75$.

is introduced, a non-zero horizontal force rises and points towards the negative x-direction, from the high to the low pressure side of the wedge. Such an horizontal force is generated by a pressure unbalance between the two sides of the wedge, clearly visible from Figs. 8–10. We also comment that, in the case of symmetric impact ($\tau = 0$ and $\theta = 0$) and the numerical model correctly returns $C_{F_x} = 0$. For all the τ values $|C_{F_x}|$ increases with θ. The trend is linear for $\theta \leq 19^{\circ}$. This situation corresponds to the flow configuration depicted in Fig. 7(a–d), that is for completely attached configurations. Notably, in partially ventilating configurations, the C_{F_x} is insensitive to τ. This means that, while on the high pressure side C_p is reduced increasing τ (see Fig. 8), on the low pressure side the size of the low pressure bubble increases as evidenced in Fig. 10. When the flow transition to type B is completed, $|C_{F_x}|$ suddenly decreases because, as the cavity opens, $p = p_{\infty}$ on the low pressure side. As expected, $|C_{Fx}|$ increases with τ. Such a dependency is larger at low θ and saturates for $\theta \geq 9^{\circ}$.

The vertical force coefficient is reported in Fig. 13b as a function of θ and τ. The kinematic asymmetry has a minor impact on C_{F_y}. Only for $\tau = 0.75$ C_{F_y} is appreciably lower compared to the other cases. On the contrary, θ dominates the C_{F_y} behavior. In fact, the larger is θ, the lower will be the effective deadrise angle on the pressure side of the wedge, and, in turn the larger is the wetted surface for a fixed penetration as evidenced in Fig. 7. The effect of the effective deadrise angle is coherent with symmetric impacts (Wagner, 1932). In conclusion, the vertical hydrodynamic force behavior for asymmetrical and symmetrical water impacts is similar, being C_{F_y} largely determined by the pressure on the high pressure side of the wedge. This can be explained by observing from Figs. 7–10 that, not only C_p, but also the effective wetted area is much larger on the high pressure side of the wedge with respect to the low pressure one.

The C_{Mz} trends are shown in Fig. 13c. For $\theta \leq 19^{\circ}$ the moment generation is largely dominated by the geometrical asymmetry and the effect of τ is negligible. Further increasing θ, for partially ventilating flows, there is a systematic drop in C_{Mz}, followed by a recovery at higher θ values, except for $\tau = 0$. Such a recovery is much faster for $\tau = 0.25$ and $\tau = 0.5$, thus producing an increment of C_{Mz} at $\theta = 30^{\circ}$ of about 50%, compared to the case with $\tau = 0.75$. This again could be related to the type B flow occurrence.

6. Conclusions

In this paper, the 2D hydrodynamics generated by the asymmetric water impact of a wedge-like section was numerically investigated. The free-surface flow modeling is based on a finite volume VOF implementation, with a special numerical treatment to avoid artificial smearing of the air-water interface across the computational domain. The study was focused on the influence of geometrical and kinematic asymmetries on the impact hydrodynamics and includes a preliminary assessment on the adopted numerical setup.

The preliminary analysis showed a high sensitivity of the computed flow with respect to the numerical domain initialization. More in details, to correctly predict flow splitting at the keel a free path prior to water impact should be introduced. This was found to be fundamental for the prediction of ventilation on the low pressure side of the wedge, thus

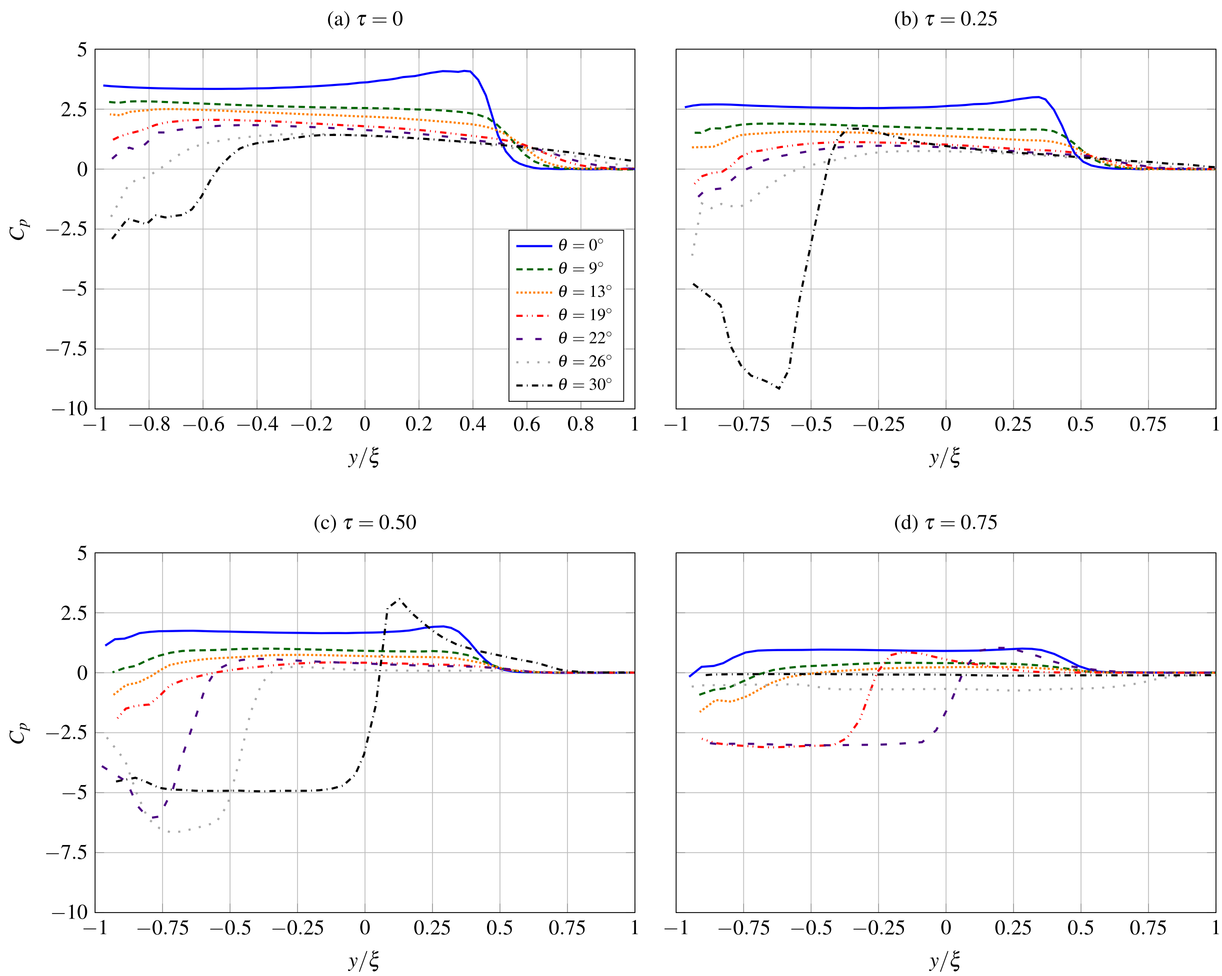

Fig. 10. Pressure profile on the wetted surface of the wedge as a function of θ and τ, low pressure side, $t = 2$ ms.

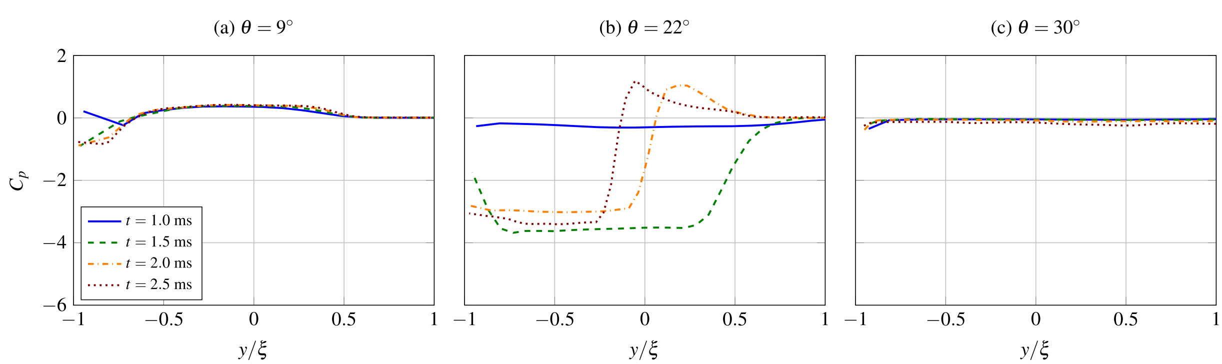

Fig. 11. Pressure coefficient on the low pressure side of the wedge as a function of time and y/ξ, for $\tau = 0.75$.

providing a useful information for the practical setup of such type of numerical simulations. A comparison between CFD and experimental data available in literature demonstrated the reliability of the proposed numerical method in predicting the wetted lengths and the transition from non-ventilating to ventilating flow conditions, as functions of the kinematic and geometrical asymmetry.

The validated methodology was used to investigate fluid forces and pressure field variations with respect to the asymmetry angle θ and the kinematic asymmetry ratio τ. The horizontal force generation strongly depends on the level of asymmetry introduced: for $\theta < 19^\circ$ both parameters affect the horizontal force coefficient value, while, above this threshold, the θ influence becomes largely dominant. The vertical force coefficient appears to be weakly dependent on the kinematic asymmetry, showing a nonlinear increase with θ and a nearly self-similar trend for the considered τ values. The tilting moment coefficient has a characteristic drop-and-recovery trend for $\tau > 0$, with the drop located approximately at $\theta = 22^\circ$. Prior to the drop point, there is very small τ dependence, while, after that, the recovery is faster for lower τ values. The slow recovery for $\tau = 0.75$ might be explained by transition to fully ventilated low-pressure side.

The pressure distribution on the wedge surface is essentially self similar on the high-pressure side, which is consistent with previous theoretical and numerical findings on symmetric impact cases. The low-pressure side has a less predictable behavior, due to the changes in the

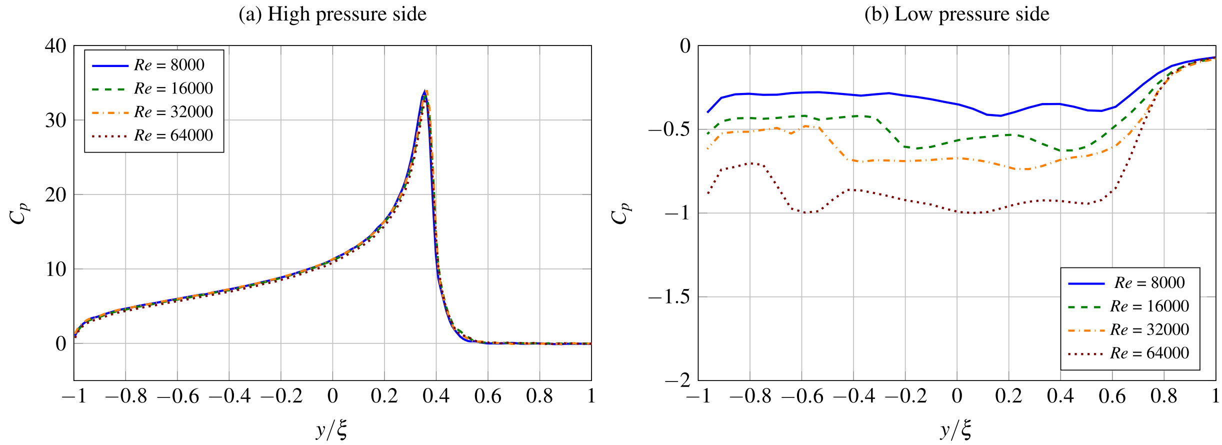

Fig. 12. Reynolds number effect on the pressure profile, $\tau = 0.75, \theta = 26°$,.

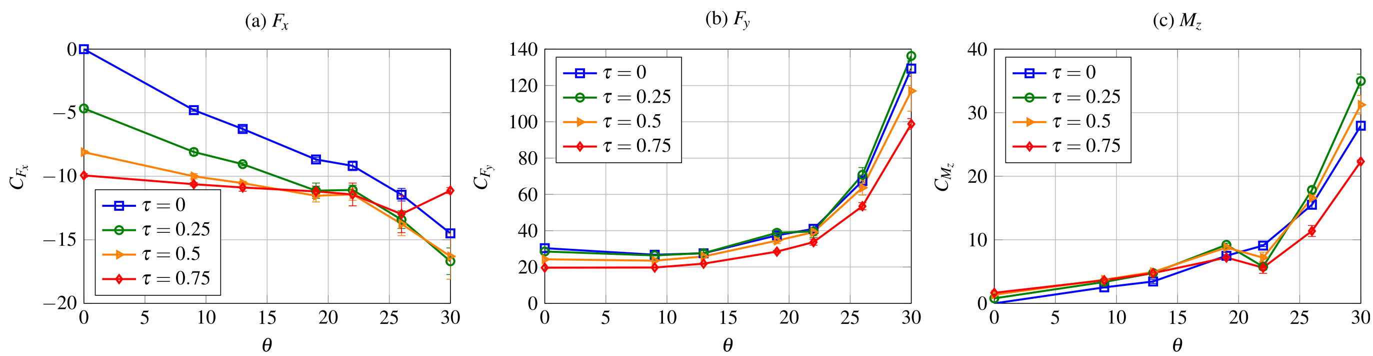

Fig. 13. Hydrodynamic force coefficients as functions of τ and θ; maximum deviations from the fitted values are also reported.

flow regime depending on the impact asymmetry level. For small θ and τ the flow remains attached and with a pressure drop close to the keel. At intermediate θ and τ the pressure drop becomes stronger and a dynamic flow separation-reattachment process occurs. When θ and τ get both large the separation dominates and the low-pressure side becomes fully ventilated with a pressure recovery towards the atmospheric value. The effect of *Re* is negligible on the high-pressure side and appears to be relatively weak also on the low-pressure side, even for transitional configurations.

Overall, the hydrodynamic load characteristics of wedge-like sections during asymmetric water entry seems to be mostly governed by the geometrical parameters of the impact, which essentially determine vertical force and tilting moment coefficients. The kinematic asymmetry is less important in the main integral force components generation, but produces significant local fluid dynamics phenomena that may lead to sudden liquid flow separation and air entrainment on the low pressure side of the wedge.

Future studies should be focused on coupled analysis of the fluid-structure interaction for asymmetric impacts, including the eventual influence of flow ventilation on such analysis.

Acknowledgements

The authors are grateful to Prof. Carolyn Judge for the useful data exchange about the reference experimental conditions used in the validation Section of the paper. This work was supported by the SCIRE Consortium (Scientific Consortium for the Industrial Research and Engineering) research contract “Sviluppo di modelli numerici di interazione fluido-struttura” and by the Italian Ministry of Education, University and Research under PRIN grant No. 20154EHYW9 “Combined numerical and experimental methodology for fluid structure interaction in free surface flows under impulsive loading”.

References

Abrate, S., 2011. Hull slamming. Appl. Mech. Rev. 64 (6). https://doi.org/10.1115/1.4023571.
Battley, M., Allen, T., 2012. Servo-hydraulic system for controlled velocity water impact of marine sandwich panels. Exp. Mech. 52 (1), 95–106. https://doi.org/10.1007/s11340-011-9543-7.
Carrica, P., Huang, J., Noack, R., Kaushik, D., Smith, B., Stern, F., 2010. Large-scale DES computations of the forward speed diffraction and pitch and heave problems for a surface combatant. Comput. Fluids 39 (7), 1095–1111. https://doi.org/10.1016/j.compfluid.2010.02.002.
Cavalagli, N., Biscarini, C., Facci, A.L., Ubertini, F., Ubertini, S., 2017. Experimental and numerical analysis of energy dissipation in a sloshing absorber. J. Fluids Struct. 68, 466–481.
Charca, S., Shafiq, B., Just, F., 2009. Repeated slamming of sandwich composite panels on water. J. Sandw. Struct. Mater. 11 (5), 409–424. https://doi.org/10.1177/1099636209103169.
Chekin, B.S., 1989. The entry of a wedge into an incompressible fluid. J. Appl. Math. Mech. 53 (3), 300–307. https://doi.org/10.1016/0021-8928(89)90026-9.
Chung, M.-H., 2013. An adaptive Cartesian cut-cell/level-set method to simulate incompressible two-phase flows with embedded moving solid boundaries. Comput. Fluids 71, 469–486. https://doi.org/10.1016/j.compfluid.2012.11.002.
Cointe, R., 1989. Two-dimensional water-solid impact. J. Offshore Mech. Arct. Eng. 111 (3), 109–114. https://doi.org/10.1115/1.3257083.
Cointe, R., Armand, J.L., 1987. Hydrodynamic impact analysis of a cylinder. J. Offshore Mech. Arct. Eng. 109 (3), 237–243. https://doi.org/10.1115/1.3257015.
Cointe, R., 1991. Free-surface flows close to a surface-piercing body. In: Miloh, T. (Ed.), Mathematical Approaches in Hydrodynamics. Soc. Industr. Appl. Math, Philadelphia, pp. 319–334.
Dobrovol'skaya, Z.N., 1969. On some problems of similarity flow of fluid with a free surface. J. Fluid Mech. 36 (4), 805–829. https://doi.org/10.1017/S0022112069001996.
Facci, A.L., Ubertini, S., 2015. Numerical assessment of similitude parameters and dimensional analysis for water entry problems. Math. Problems Eng. 15. https://doi.org/10.1155/2015/324961. Article ID 324961.
Facci, A.L., Panciroli, R., Ubertini, S., Porfiri, M., 2015. Assessment of PIV-based analysis of water entry problems through synthetic numerical datasets. J. Fluids Struct. 55, 484–500. https://doi.org/10.1016/j.jfluidstructs.2015.03.018.

Facci, A.L., Porfiri, M., Ubertini, S., 2016. Three-dimensional water entry of a solid body: a computational study. J. Fluids Struct. 66, 36–53. https://doi.org/10.1016/j.jfluidstructs.2016.07.015.
Falcucci, G., Aureli, S., Ubertini, S., Porfiri, M., 2011. Transverse harmonic oscillations of laminæ in viscous fluids: a lattice Boltzmann study. Phil. Trans. R. Soc. A 369, 2456–2466. https://doi.org/10.1098/rsta.2011.0062.
Faltinsen, O., 1993. Sea Loads on Ships and Offshore Structures, vol. 1. Cambridge University Press, Cambridge, UK.
Faltinsen, O.M., Landrini, M., Greco, M., 2004. Slamming in marine applications. J. Eng. Math. 48 (3–4), 187–217. https://doi.org/10.1023/B:engi.0000018188.68304.ae.
Ferziger, J.H., Perić, M., 2002. Computational Methods for Fluid Dynamics, third rev. ed. Springer-Verlag, Berlin-Tokyo.
Greenhow, M., 1987. Wedge entry into initially calm water. Appl. Ocean Res. 9 (4), 214–223. https://doi.org/10.1016/0141-1187(87)90003-4.
Greenshields, C.J., 2015a. OpenFOAM Programmer's Guide, second ed. OpenFOAM Foundation Ltd.
Greenshields, C.J., 2015b. OpenFOAM User's Guide, second ed. OpenFOAM Foundation Ltd.
Gu, X., Moan, T., 2002. Long-term fatigue damage of ship structures under nonlinear wave loads. Mar. Technol. 39 (2), 95–104.
Gu, H.B., Qian, L., Causon, D.M., Mingham, C.G., Lin, P., 2014. Numerical simulation of water impact of solid bodies with vertical and oblique entries. Ocean. Eng. 75, 128–137.
Hirt, C.W., Nichols, B.D., 1981. Volume of fluid (VOF) method for the dynamics of free boundaries. J. Comput. Phys. 39 (1), 201–225. https://doi.org/10.1016/0021-9991(81)90145-5.
Howinson, S.D., Ockendon, J.R., Wilson, S.K., 1991. Incompressible water-entry problems at small deadrise angles. J. Fluid Mech. 222, 215–230. https://doi.org/10.1017/S0022112091001076.
Issa, R.I., 1985. Solution of the implicitly discretized fluid flow equations by operator-splitting. J. Comput. Phys. 62, 40–65. https://doi.org/10.1016/0021-9991(86)90099-9.
Jalalisendi, M., Osma, S.J., 2015. Three-dimensional water entry of a solid body: a particle image velocimetry study. J. Fluids Struct. 59, 85–102. https://doi.org/10.1016/j.jfluidstructs.2015.08.013.
Jalalisendi, M., Shams, A., Panciroli, R., Porfiri, M., 2015. Experimental reconstruction of three-dimensional hydrodynamic loading in water entry problems through particle image velocimetry. Exp. Fluids 56 (2), 1–17. https://doi.org/10.1007/s00348-015-1895-9.
H. Jasak, Dynamic mesh handling in OpenFOAM, 47th AIAA Aerospace Sciences Meeting Including the New Horizons Forum and Aerospace Exposition, 5–8 January 2009, Orlando, Florida.
Jasak, H., Tukovic, Z., 2007. Automatic mesh motion for the unstructured finite volume method. Trans. FAMENA 30, 1–18.
Jasak, H., Weller, H., Gosman, A., 1999. High resolution nvd differencing scheme for arbitrarily unstructured meshes. Int. J. Numer. Methods Fluids 31 (2), 431–449. https://doi.org/10.1002/(SICI)1097-0363(19990930)31:2<431::AID-FLD884>3.0.CO;2-T.
De Jouëtte, C., Laget, O., Le Gouez, J.-M., Viviand, H., 2001. A dual time stepping method for fluid–structure interaction problems. Comput. Fluids 31 (4–7), 509–537. https://doi.org/10.1016/S0045-7930(01)00068-8.
C. Judge, Personal Communications with the Authors.
Judge, C., Troesch, A., Perlin, M., 2004. Initial water impact of a wedge at vertical and oblique angles. J. Eng. Math. 48 (3-4), 279–303. https://doi.org/10.1023/B:engi.0000018187.33001.e1.
Von Kármán, T., 1929. The Impact on Seaplane Floats during Landing. NACA TN 321.
Kassiotis, C., 2008. Which Strategy to Move the Mesh in the Computational Fluid Dynamic Code OpenFOAM? Tech. rep., WiRe, LMT-Cachan, Germany, France, 2008. http://perso.crans.org/kassiotis/openfoam/movingmesh.pdf.
Kelecy, F.J., Pletcher, R.H., 1997. The development of a free surface capturing approach for multidimensional free surface flows in closed containers. J. Comput. Phys. 138 (2), 939–989. https://doi.org/10.1006/jcph.1997.5847.
Korobkin, A.A., 1988. Inclined entry of a blunt profile into an ideal fluid. Fluid Dyn. 23 (3), 443–447. https://doi.org/10.1007/BF01054755.
Lewis, S.G., Hudson, D.A., Turnock, S.R., Taunton, D.J., 2010. Impact of a free-falling wedge with water: synchronized visualization, pressure and acceleration measurements. Fluid Dyn. Res 42 (3).
Lu, C.H., He, Y.S., Wu, G.X., 2000. Coupled analysis of nonlinear interaction between fluid and structure during impact. J. Fluids Struct. 14, 127–146. https://doi.org/10.1006/jfls.1999.0257.
Ma, Z., Causon, D., Qian, L., Gu, H., Mingham, C., Martínez Ferrer, P., 2015. A GPU based compressible multiphase hydrocode for modelling violent hydrodynamic impact problems. Comput. Fluids 120, 1–23. https://doi.org/10.1016/j.compfluid.2015.07.010.
Miloh, T., 1991. On the oblique water-entry problem of a rigid sphere. J. Eng. Math. 25, 77–92. https://doi.org/10.1007/BF00036603.
Oger, G., Doring, M., Alessandrini, B., Ferrant, P., 2006. Two-dimensional SPH simulations of wedge water entry. J. Comput. Phys. 213 (2), 803–822. https://doi.org/10.1016/j.jcp.2005.09.004.
OpenFOAM, www.openfoam.com (2015).
Osher, S., Sethian, J.A., 1988. Fronts propagating with curvature-dependent speed: algorithms based on Hamilton–Jacobi formulations. J. Comput. Phys. 79 (1), 12–49. https://doi.org/10.1016/0021-9991(88)90002-2.
Panciroli, R., Porfiri, M., 2013. Evaluation of the pressure field on a rigid body entering a quiescent fluid through particle image velocimetry. Exp. fluids 54 (12), 1–13. https://doi.org/10.1007/s00348-013-1630-3.
Panciroli, R., Biscarini, C., Falcucci, G., Jannelli, E., Ubertini, S., 2015. Live monitoring of the distributed strain field in impulsive events through fiber bragg gratings. J. Fluids Struct. 61, 60–75. https://doi.org/10.1016/j.jfluidstructs.2015.10.013.
Panciroli, R., Shams, A., Porfiri, M., 2015. Experiments on the water entry of curved wedges: high speed imaging and particle image velocimetry. Ocean. Eng. 94, 213–222. https://doi.org/10.1016/j.oceaneng.2014.12.004.
Rider, W.J., Kothe, D.B., 1998. Reconstructing volume tracking. J. Comput. Phys. 141 (2), 112–152. https://doi.org/10.1006/jcph.1998.5906.
De Rosis, A., Falcucci, G., Porfiri, M., Ubertini, S., Ubertini, F., 2014. Hydroelastic analysis of hull slamming coupling lattice Boltzmann and finite element methods. Comput. Struct. 138, 24–35. https://doi.org/10.1016/j.compstruc.2014.02.007.
Rusche, H., 2002. Computational Fluid Dynamiccs of Dispersed Two-phase Flows at High Phase Fractions. Ph.D. thesis.
Russo, S., Krastev, V.K., Jannelli, E., Falcucci, G., 2016. Design and optimization of an experimental test bench for the study of impulsive fluid-structure interactions. In: AIP Conference Proceedings, vol. 1738, p. 270020. https://doi.org/10.1063/1.4952059.
Russo, S., Biscarini, C., Facci, A.L., Falcucci, G., Jannelli, E., Ubertini, S., 2017. Experimental assessment of buoyant cylinder impacts through high-speed image acquisition. J. Mar. Sci. Technol. 1–14.
Scardovelli, R., Zaleski, S., 1999. Direct numerical simulation of free-surface and interfacial flow. Annu. Rev. Fluid Mech. 31 (1), 567–603. https://doi.org/10.1146/annurev.fluid.31.1.567.
Seddon, C., Moatamedi, M., 2006. Review of water entry with applications to aerospace structures. Int. J. Impact Eng. 32 (7), 1045–1067. https://doi.org/10.1016/j.ijimpeng.2004.09.002.
Seng, S., Jensen, J.J., Pedersen, P.T., 2012. Numerical prediction of slamming loads. Proc. Inst. Mech. Eng. Part M J. Eng. Marit. Environ. 226 (2), 120–134.
Shadloo, M.S., Oger, G., Le Touzé, D., 2016. Smoothed particle hydrodynamics method for fluid flows, towards industrial applications: motivations, current state, and challenges. Comput. Fluids 136, 11–34. https://doi.org/10.1016/j.compfluid.2016.05.029.
Shams, A., Jalalisendi, M., Porfiri, M., 2015. Experiments on the water entry of asymmetric wedges using particle image velocimetry. Phys. Fluids 27 (2). https://doi.org/10.1063/1.4907745.
Shao, S., Ji, C., Graham, D.I., Greeve, D.E., James, P.W., Chadwik, A.J., 2006. Simulation of wave overtopping by an incompressible SPH model. Coast. Eng. 53 (9), 723–735. https://doi.org/10.1016/j.coastaleng.2006.02.005.
Silva, M.L., Ravichandran, G., 2012. Stress field evolution under mechanically simulated hull slamming conditions. Exp. Mech. 52 (1), 107–116. https://doi.org/10.1007/s11340-011-9529-5.
Tveitnes, T., Fairlie-Clarke, A.C., Varyani, K., 2008. An experimental investigation into the constant velocity water entry of wedge-shaped sections. Ocean. Eng. 35 (14), 1463–1478. https://doi.org/10.1016/j.oceaneng.2008.06.012.
Wagner, H., 1932. Über stoß- und gleitvorgänge an der oberfläche von flüssigkeiten. ZAMM 12 (4), 193–215.
Wu, G.X., 2007. Fluid impact on a solid boundary. J. Fluids Struct. 23, 755–765. https://doi.org/10.1016/j.jfluidstructs.2006.11.002.
Wu, G.X., Sun, H., He, Y.S., 2004. Numerical simulation and experimental study of water entry of a wedge in free fall motion. J. Fluids Struct. 19, 277–289. https://doi.org/10.1016/j.jfluidstructs.2004.01.001.
Xu, G.D., Duan, W.Y., Wu, G.X., 2008. Numerical simulation of oblique water entry of an asymmetrical wedge. Ocean. Eng. 35, 1597–1603. https://doi.org/10.1016/j.oceaneng.2008.08.002.
A. Zarghami, G. Falcucci, E. Jannelli, S. Succi, M. Porfiri, S. Ubertini, Lattice Boltzmann modeling of water entry problems, Int. J. Mod. Phys. C 25(12). https://doi.org/10.1142/S0129183114410125.
Zhao, R., Faltinsen, O.M., 1993. Water entry of two-dimensional bodies. J. Fluid Mech. 246, 593–612. https://doi.org/10.1017/S002211209300028X.